Exposure Levels Induced in Curved Body Parts at mmWaves

Giulia Sacco, Zain Haider, Maxim Zhadobov

To cite this version:

Giulia Sacco, Zain Haider, Maxim Zhadobov. Exposure Levels Induced in Curved Body Parts at mmWaves. IEEE Journal of Electromagnetics, RF and Microwaves in Medicine and Biology, 2022, 6 (3), pp.413-419. 10.1109/JERM.2022.3178604 . hal-03771483

HAL Id: hal-03771483
https://hal.science/hal-03771483

Submitted on 16 Sep 2022

Exposure Levels Induced in Curved Body Parts at mmWaves

Giulia Sacco, *Member, IEEE*, Zain Haider, and Maxim Zhadobov, *Senior Member, IEEE*

***Abstract*—This study investigates the impact of the ear and the finger curvature on the electromagnetic (EM) power absorption and resulting heating to quantify the potential enhancement of the induced exposure levels compared to commonly used planar tissue models. The analysis is performed at millimeter-wave (mmW) frequencies upcoming for 5G and future generations, with a special attention to 26 GHz and 60 GHz. A cylindrical model is used to calculate EM power density and heat in fingers (radii $a \leq 10\,\mathrm{mm}$) and EM power density in ears ($1\,\mathrm{mm} \leq a \leq 5\,\mathrm{mm}$). To compute the temperature rise in the ear, the model is modified to account for heat conduction in the tissue connecting the ear to the head. Our results show that for transverse electric (TE) polarization the maximal absorbed power density remains generally lower than for a planar interface (up to $-38.2\,\%$ at $26\,\mathrm{GHz}$ and $-18.7\,\%$ at $60\,\mathrm{GHz}$) and exceeds this value for transverse magnetic (TM) polarization (up to $72.3\,\%$ at $26\,\mathrm{GHz}$ and $15\,\%$ at $60\,\mathrm{GHz}$). The resulting heating is always higher than for the planar model. For the ear model ($a = 1\,\mathrm{mm}$), the variations at steady state reach $93.11\,\%$ at $26\,\mathrm{GHz}$ and $103.62\,\%$ at $60\,\mathrm{GHz}$.**

***Index Terms*—Curved phantoms, dosimetry, fifth-generation (5G), mmW.**

I. INTRODUCTION

WITH the upcoming massive deployment of 5G, wireless networks are expected to be heterogeneous in terms of frequency and coverage. Several countries have already proceeded to deploy millimeter-wave (mmW) small cells in the 24–28 GHz range (just below the mmW region starting at $30\,\mathrm{GHz}$ [1], [2]) and are devoting a great attention to frequencies around $60\,\mathrm{GHz}$ [3], [4]. Wireless devices operating in these bands are already available on the market [5], [6]. At these frequencies, the absorption in the human body is mainly superficial due to a shallow penetration depth [7]. Most of dosimetry studies performed in this range employed planar monolayer [8], [9] or multilayer [10]–[14] tissue-equivalent electromagnetic (EM) models. However, for some body parts where the wavelength in the skin is comparable with their curvature radius, the planar approximation may result in an unrealistic estimation of the exposure levels.

Some reports investigated the impact of the curvature radius in the 900MHz–3.7GHz range [15] on human hands exposure and body-centric propagation at $60\,\mathrm{GHz}$ [16]. A recent study considered $2\,\mathrm{cm}$ to $5\,\mathrm{cm}$ curvature radii to analyze exposure levels induced in an arm model from $6\,\mathrm{GHz}$ to $60\,\mathrm{GHz}$ [17]. However, for some body parts (such as finger or ear located in the vicinity of mobile devices during a call or browsing) the curvature radii are of several mm.

The exponential decrease of the field intensity inside a soft tissue can only be valid at frequencies where the ratio between the curvature radius a and penetration depth δ exceeds a factor of 5 (typically in the skin $a > 19\,\mathrm{mm}$ at $10\,\mathrm{GHz}$, $a > 5\,\mathrm{mm}$ at $26\,\mathrm{GHz}$, $a > 2.39\,\mathrm{mm}$ at $60\,\mathrm{GHz}$) [18]. This is due to constructive/destructive interference of the EM field in tissues for smaller a.

The aim of this study is to investigate the impact of the ear and finger curvature on the EM power absorption and heating compared to the conventional planar tissue models. The analysis is performed at the frequencies upcoming for 5G and future generations of mobile networks [3], [19], with a special emphasis on $26\,\mathrm{GHz}$ and $60\,\mathrm{GHz}$ (for the sake of simplicity referred in the rest of the paper as mmW since at $26\,\mathrm{GHz}$ the interactions between EM fields and human tissues are similar to those at mmW).

II. MATERIALS AND METHODS

A. *Exposure Scenario*

Ears and fingers are among the most exposed body parts since they are in contact or in proximity of wireless devices during browsing or phone calls. For these body parts with relatively small radii (compared for instance to arms, torso or head), the penetration depth at mmW is comparable to the typical curvature radii. In this case, planar models may result in an inaccurate evaluation of the exposure levels. We considered two 2D models representing in 3D (Fig. 1): (1) an infinite cylinder (Phantom 1); (2) an infinite cylinder extended along x axis (Phantom 2).

The latter is obtained by adding to the cylinder a parallelepiped with a rectangular section ($l \times 2a$, $l = 7\,\mathrm{cm}$). In the EM study, the finger and the external parts of the ear are represented by Phantom 1. The 1–5 mm range is considered as a typical range of curvature radii of the ear, while $a \leq 10\,\mathrm{mm}$ corresponds to the typical radii of the finger [20], [21]. Note that due to the shallow penetration depth the effect of the curvature is

---

Manuscript received January 13, 2022; revised March 13, 2022 and April 19, 2022; accepted May 16, 2022. This work was supported in part by the European Union's Horizon 2020 Research and Innovation Programme under the Marie Skłodowska-Curie Grant Agreement 899546 and in part by the French National Research Program for Environmental and Occupational Health of ANSES under Grant 2018/2 RF/07 through NEAR 5G project. *(Corresponding author: Giulia Sacco.)*

The authors are with the IETR (Institut d'Électronique et des Technologies du numéRique), University of Rennes 1 CNRS, UMR 6164, F-35000 Rennes, France (e-mail: giulia.sacco.it@gmail.com; zain.haider@univ-rennes1.fr; maxim.zhadobov@univ-rennes1.fr).

Digital Object Identifier 10.1109/JERM.2022.3178604

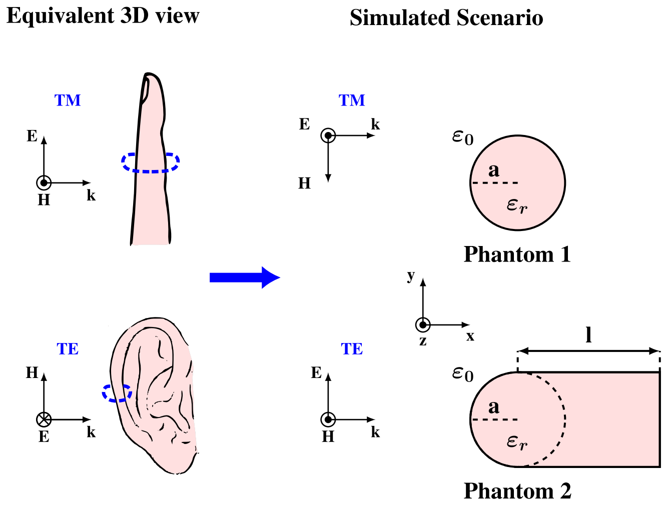

Fig. 1. Exposure scenarios.

of importance only for the external part of the ear, which can be locally represented by a cylinder. Due to thermal conduction, the heat propagates deeper into tissues compared to the EM power. Therefore, in the thermal analysis we used Phantom 2 to model the ear.

The EM problem is solved analytically and numerically considering an impinging plane wave with the $\boldsymbol{E}$ field parallel [TM polarization] and perpendicular [transverse electric (TE) polarization] to the cylinder axis. The complex permittivity of the phantom is that of human dry skin ($17.71 - j16.87$ at 26 GHz and $7.98 - j10.90$ at 60 GHz [22]). Due to the symmetry of the considered phantoms, 2D models are used to reduce the computational cost.

B. Analytical Model

The EM analytical solution is obtained considering the scattering from an infinite dielectric cylinder [23]. The incident fields can be expressed in cylindrical coordinates as

$$\boldsymbol{E}_{\text{inc}}^{\text{TM}} = \hat{\boldsymbol{z}} E_{\text{z,inc}}^{\text{TM}} = E_0 \sum_{n=N_{min}}^{N_{max}} j^{-n} J_n(k_0 \rho)\, e^{jn\phi} \tag{1a}$$

$$\boldsymbol{H}_{\text{inc}}^{\text{TE}} = \hat{\boldsymbol{z}} H_{\text{z,inc}}^{\text{TE}} = H_0 \sum_{n=N_{min}}^{N_{max}} j^{-n} J_n(k_0 \rho)\, e^{jn\phi}\,, \tag{1b}$$

for TE and TM plane waves, respectively, where E_0 and H_0 are the amplitudes of the corresponding incident fields, J_n is the Bessel function of order n, k_0 is the wave number in free space, z, ρ and ϕ are the cylindrical coordinates. The starting and ending values of the summation for the following analysis have been set to $N_{max} = -N_{min} = 80$. These values are chosen to ensure the formation of a plane wave and approximate accurately the field inside the cylinder section when considering a radius representative of ears and fingers (a in the 1–10 mm range). The field inside the cylinder is expressed as

$$\boldsymbol{E}_{\text{int}}^{\text{TM}} = \hat{\boldsymbol{z}} E_{\text{z,inc}}^{\text{TM}} = E_0 \sum_{n=-Nmin}^{Nmax} c_n J_n(k_r \rho)\, e^{jn\phi} \tag{2a}$$

$$\boldsymbol{H}_{\text{int}}^{\text{TE}} = \hat{\boldsymbol{z}} H_{\text{z,inc}}^{\text{TE}} = H_0 \sum_{n=-Nmin}^{Nmax} d_n J_n(k_r \rho)\, e^{jn\phi} \tag{2b}$$

where

$$c_n = \frac{2 j^{-(n+1)} / (\pi k_0 a)}{H_n^{(2)\prime}(k_0 a)\, J_n(k_r a) - \sqrt{\varepsilon_r} H_n^{(2)}(k_0 a)\, J_n'(k_r a)}\,, \tag{3a}$$

$$d_n = \frac{2 \sqrt{\varepsilon_r} j^{-(n+1)} / (\pi k_0 a)}{\sqrt{\varepsilon_r} H_n^{(2)\prime}(k_0 a)\, J_n(k_r a) - H_n^{(2)}(k_0 a)\, J_n'(k_r a)}\,, \tag{3b}$$

k_r and ε_r are the wave number and permittivity of the skin and $H_n^{(2)}$ is the Hankel function. $\boldsymbol{H}$ field for the TM polarization and $\boldsymbol{E}$ field for the TE polarization are computed with the Maxwell's equations [23]. The absorbed power density (APD) is calculated as [24]

$$\boldsymbol{APD} = \frac{1}{2} Re \left[\boldsymbol{E} \times \boldsymbol{H}^* \right] \cdot \hat{\boldsymbol{n}} \tag{4}$$

and the power loss density (PLD) as [24], [25]

$$PLD = \sigma_{skin} \left| \boldsymbol{E}_{\text{rms}} \right|^2 \,, \tag{5}$$

where $\hat{\boldsymbol{n}}$ is the normal to the surface of the cylinder, σ_{skin} is the skin conductivity and the $\boldsymbol{E}_{\text{rms}}$ is the root mean square value of the $\boldsymbol{E}$ field.

C. Numerical Model

To validate the analytical results, we used the finite element method (FEM) implemented in COMSOL Multiphysics. A perfectly matched layer (PML) with a thickness of 3λ is positioned around the structure to reproduce the free-space condition. To further eliminate the reflections at the simulation boundaries on the external side of the PML, scattering boundary conditions are added. A plane wave having the wave vector $\boldsymbol{k}$ in the x direction and the $\boldsymbol{E}$ field in the z (TM polarization) or y (TE polarization) direction is used to excite the structure. The structure is discretized with a tetrahedral mesh. The maximal mesh cell size is $\lambda/15$ in the free space and $\lambda/40$ in the phantom (corresponding to 0.07 mm at 26 GHz and 0.04 mm at 60 GHz). The total number of cells ranges from 430 000 to 700 000 at 26 GHz and from 430 000 to 1 000 000 at 60 GHz for $1\ \text{mm} \leq a \leq 10\ \text{mm}$.

An identical model is used for the thermal study to compute the temperature increase by solving the Pennes' bioheat equation [26]. The steady state (SS) and transient temperature rises are computed. The temperature distribution in the absence of the EM source is used as the initial condition for the latter. The blood flow coefficient is set to 7440 W/(m^3 K) and the skin density to 1109 kg/m^3 [27]. In addition, to simulate the heat exchange between the phantom and the surrounding environment, a convective flux is imposed at the surface of the skin with a heat transfer coefficient of 5 W/(m^2 K).

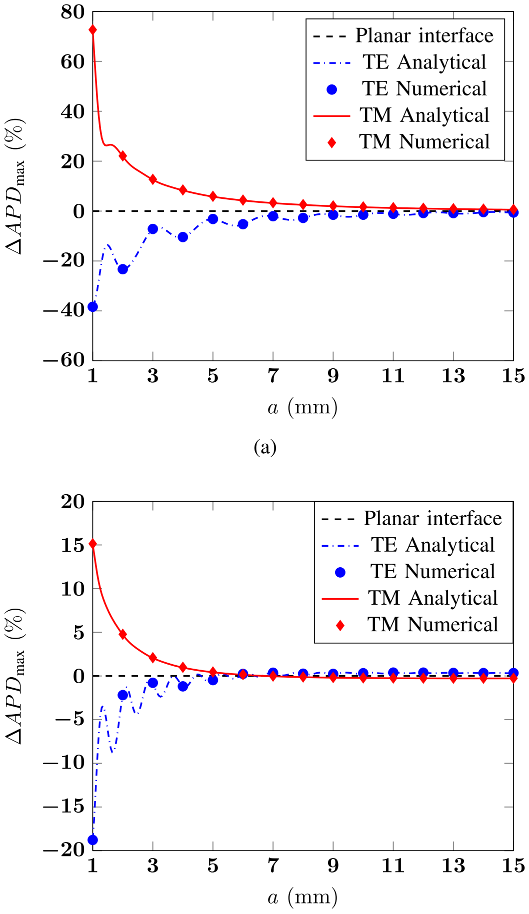

(a)

(b)

Fig. 2. Variations of the $APD_{\max}$ as a function of the curvature radius with respect to the planar interface at (a) 26 GHz and (b) 60 GHz.

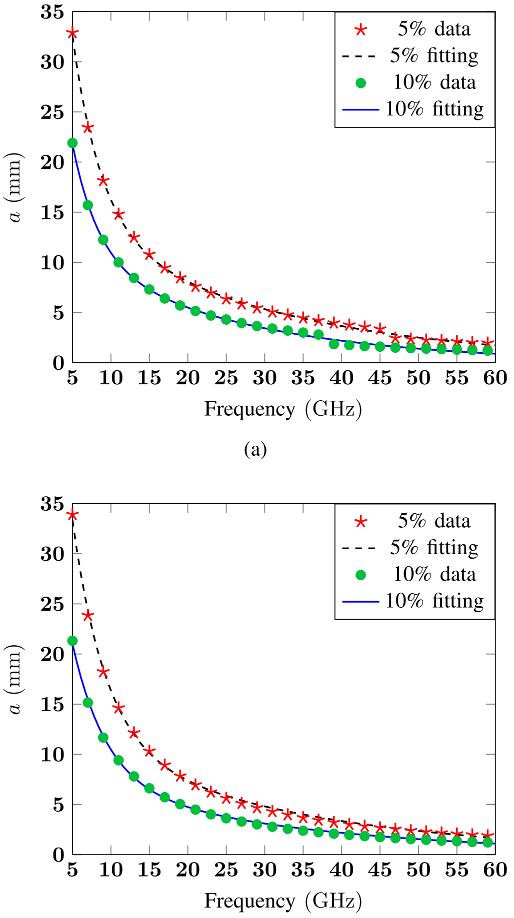

(a)

(b)

Fig. 3. Curvature radius a corresponding to $5\,\%$ or $10\,\%$ variations in terms of $APD_{\max}$ as a function of frequency for (a) TE polarization, and (b) TM polarization.

TABLE I

SUMMARY OF THE MAIN EM AND THERMAL RESULTS

a		**1 mm**		**5 mm**		**10 mm**	
		26 GHz	**60 GHz**	**26 GHz**	**60 GHz**	**26 GHz**	**60 GHz**
$\Delta APD_{\max}$	**TE**	–38.2%	–18.7%	–3.2%	–0.5%	–1.5%	0.3%
	TM	72.3%	15%	5.8%	0.4%	1.6%	–0.2%
$\Delta T_{\max}$ SS	**TE**	93%	103.6%	39.5%	39.4%	28.2%	27.4%
	TM	93.1%	31.7%	16.2%	3.8%	11.4%	7%

III. RESULTS

A. *Power Density*

The APD for Phantom 1 is analytically calculated and numerically computed at 26 GHz and 60 GHz. Since the considered diameters are smaller or comparable with typical dimensions of 4 cm^2 spatial-averaging area in the international guidelines [24], [25], in the following analysis we considered local APD and PLD. The peak APD ($APD_{\max}$) in the curved structures is compared to that at planar air-skin interface of a homogenous phantom (Fig. 2).

$APD_{\max}$ tends to converge to that of a planar interface for $a > 13.45\,\mathrm{mm}$ at 26 GHz and $a > 4.2\,\mathrm{mm}$ at 60 GHz [$99\,\%$ convergence]. For a tending to $1\,\mathrm{mm}$, the amplitude of $APD_{\max}$ variations increases. At both frequencies, for the TE polarization $APD_{\max}$ remains lower than for the planar interface, while for the TM polarization $APD_{\max}$ is higher. This is due to the fact that the $|\boldsymbol{E}_{\mathrm{z,int}}^{\mathrm{TM}}|$ at $(-a, 0)$ decreases when a increases and the field distribution is symmetrical with respect to xz. On the contrary, $\boldsymbol{E}_{\mathrm{x,int}}^{\mathrm{TE}}$ phases are anti-symmetrical with respect to the same axis. The ripples for the TE polarization are due to the surface waves on the cylinder. A similar behaviour was reported for the TE polarization on a perfect electric conducting cylinder [23]. At 26 GHz, the $APD_{\max}$ variation for $a = 1\,\mathrm{mm}$ corresponds to $-38.2\,\%$ for TE and $72.3\,\%$ for TM polarization. At 60 GHz, the maximal increase is $15\,\%$ (TM polarization) and the maximal decrease is $-18.7\,\%$ (TE polarization). The strongest variations for $a = 1\,\mathrm{mm}$ at 26 GHz can be attributed to the fact that at this frequency the penetration depth is higher and the phantom is electrically smaller than at 60 GHz. $\Delta APD_{\max}$ trend at the surface of the phantom is almost identical to that of $\Delta SAR_{\max}$ (data not shown for the sake of brevity). The highest deviation between $\Delta APD_{\max}$ and $\Delta SAR_{\max}$ is $+8.4\,\%$ at $a = 1.05\,\mathrm{mm}$ (26 GHz) and $-1.4\,\%$ at $a = 1.25\,\mathrm{mm}$ (26 GHz). Analytical results are in an excellent agreement with simulations.

The analysis of the variations of the $APD_{\max}$ is then extended to 5–60 GHz (frequency range upcoming for 5G and beyond [3],

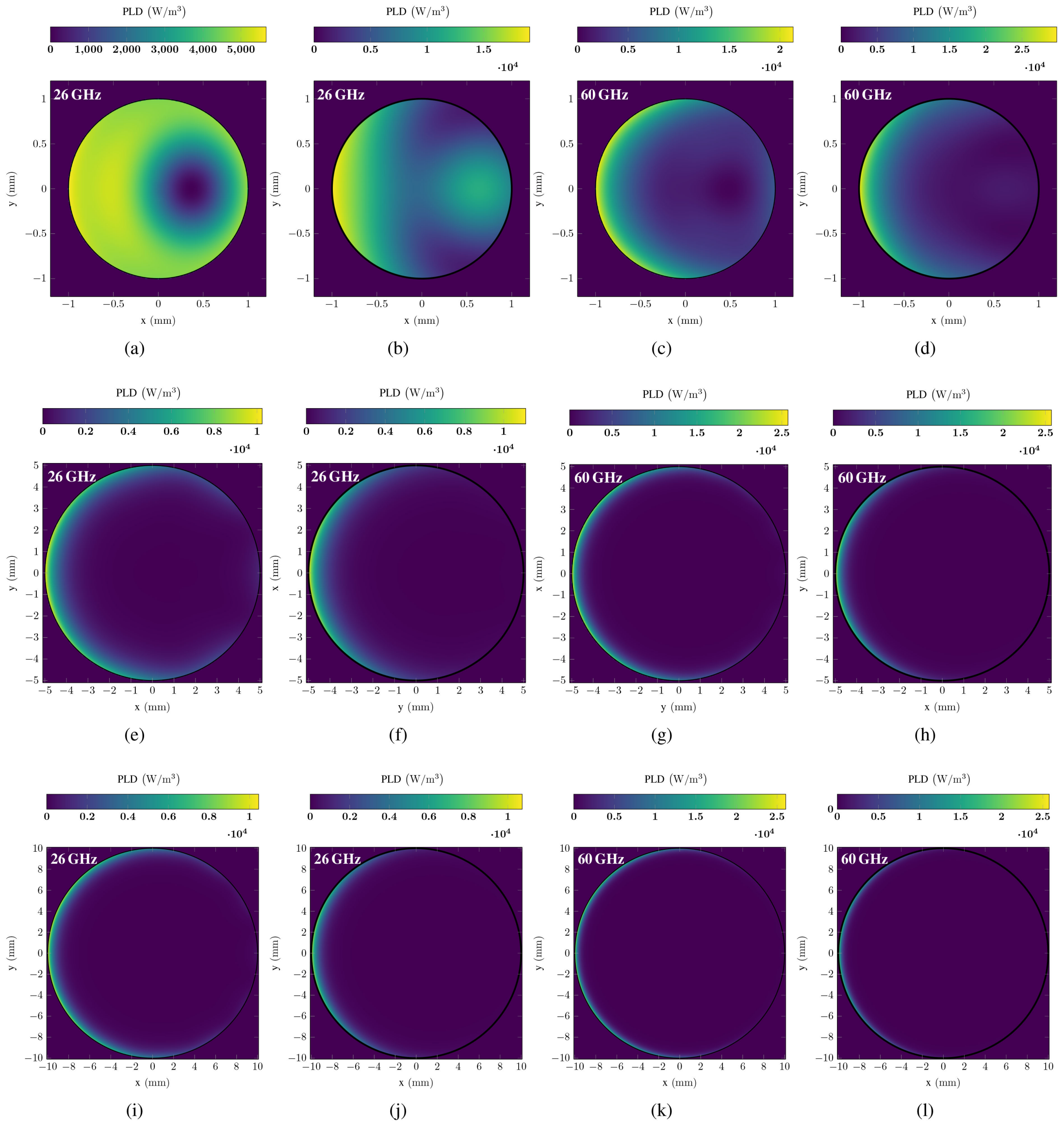

Fig. 4. PLD distribution over the cylinder section for $a = 1\,\mathrm{mm}$ [(a) TE and (b) TM polarizations at 26 GHz, (c) TE and (d) TM polarizations at 60 GHz], $a = 5\,\mathrm{mm}$ [(e) TE and (f) TM polarizations at 26 GHz, (g) TE and (h) TM polarizations at 60 GHz], and $a = 10\,\mathrm{mm}$ [(i) TE and (j) TM polarizations at 26 GHz, (k) TE and (l) TM polarizations at 60 GHz].

[19]). Fig. 3 reports the curvature radius a corresponding to $5\,\%$ and $10\,\%$ variations of $APD_{\max}$ compared to the planar interface.

These values are chosen to provide a quantitative estimate of the frequency-dependent threshold for a. Above this threshold the variations of $APD_{\max}$ may be considered negligible. The data points are computed every $1\,\mathrm{GHz}$ and interpolated with exponential functions. The functions that better approximate the data considering confidence bounds of $95\,\%$ are:

1) for TE polarization

$$a_{5\%}^{TE} = 72.4e^{-0.2678 f_{GHz}} + 16.4e^{-0.03757 f_{GHz}}\,; \tag{6a}$$

$$a_{10\%}^{TE} = 49.56e^{-0.2962 f_{GHz}} + 13.13e^{-0.0448 f_{GHz}}\,; \tag{6b}$$

2) for TM polarization

$$a_{5\%}^{TM} = 70.97e^{-0.2345 f_{GHz}} + 13.56e^{-0.03495 f_{GHz}}\,; \tag{7a}$$

$$a_{10\%}^{TM} = 43.33e^{-0.2279 f_{GHz}} + 8.481e^{-0.03403 f_{GHz}}\,. \tag{7b}$$

Interestingly, the results are almost independent of polarization. At $26\,\mathrm{GHz}$, the radii a corresponding to a $5\,\%$ variation are $6.1\,\mathrm{mm}$ (TE polarization) and $5.5\,\mathrm{mm}$ (TM polarization), the ones corresponding to $10\,\%$ variations are $4.1\,\mathrm{mm}$ (TE polarization) and $a = 3.55\,\mathrm{mm}$ (TM polarization). At 60 GHz, the radii resulting in a $5\,\%$ modification are $1.9\,\mathrm{mm}$ (TE polarization) and $1.95\,\mathrm{mm}$ (TM polarization), while the ones resulting in a $10\,\%$ variation are $1.15\,\mathrm{mm}$ (TE polarization) and $1.25\,\mathrm{mm}$ (TM polarization). It is worth noticing that these radii are comparable (for an adult) or slightly greater (for a child or a toddler) than the typical ear radius. At lower frequencies, greater radii are required to induce variations lower than $5\,\%$ or $10\,\%$. In other words, if a is comparable with the curvature radii of the ear and/or finger (i.e., $a \leq 10\,\mathrm{mm}$), the power absorption would differ by

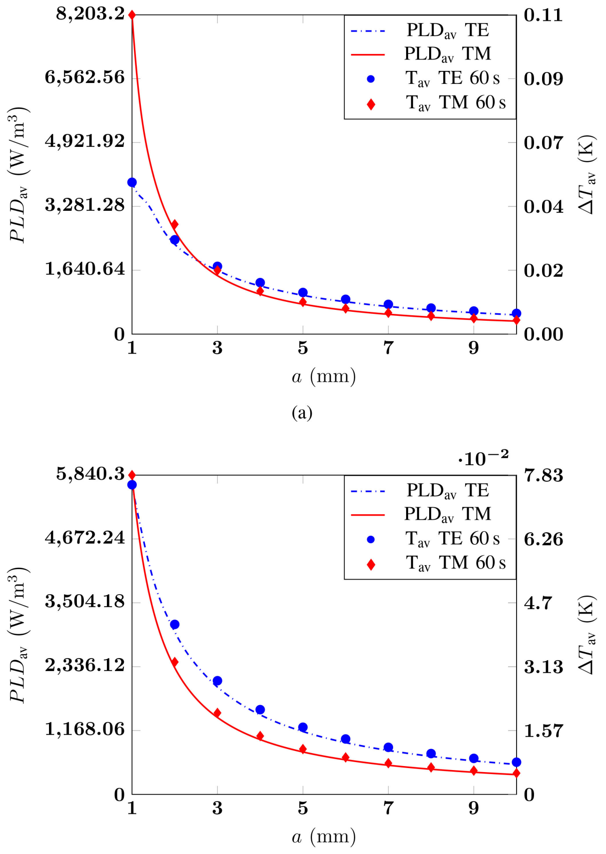

(a)

(b)

Fig. 5. PLD_{av} (left axis) and ΔT_{av} after a 60 s exposure (right axis) as a function of the curvature radius a at (a) 26 GHz and (b) 60 GHz.

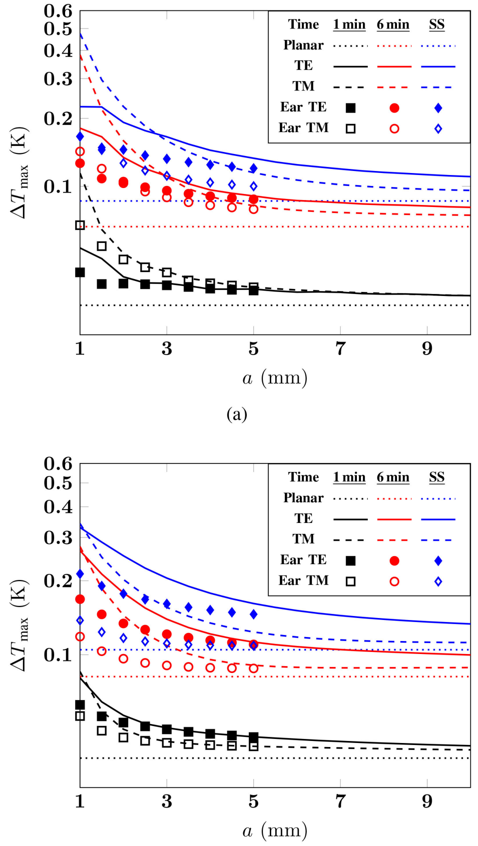

(a)

(b)

Fig. 6. $\Delta T_{\max}$ as a function of the curvature radius a for the cylindrical geometry and the one used to model the thermal diffusion in the ear at (a) 26 GHz and (b) 60 GHz.

more than $5\,\%$ or $10\,\%$ compared to the planar model. As an example, at 5 GHz a peak APD variation lower than $5\,\%$ and $10\,\%$ can be reached only for the curvature radii representative of limbs [17], e.g., for arms approximately $a = 30\,\text{mm}$ and $a = 20\,\text{mm}$, respectively. Smaller curvature radii would result in higher variations.

To get a deeper insight into the absorbed power distribution, PLD over the cylinder cross-section is computed for $a = 1\,\text{mm}$, $a = 5\,\text{mm}$, and $a = 10\,\text{mm}$ (Fig. 4).

For all a, the peak PLD occurs at the phantom surface. Due to a relatively high electrical conductivity at mmW, the absorption in essentially superficial for all the models, except for $a = 1\,\text{mm}$ at 26 GHz. This is a consequence of the fact that at this frequency the penetration depth is about $1\,\text{mm}$, which is comparable with the curvature radius.

B. Temperature Rise

The temperature rise associated to the EM exposure is computed for $1\,\text{min}$ and $6\,\text{min}$ of exposure as well as at SS, which is reached after about 30–40 min of exposure. Although $6\,\text{min}$ is the duration chosen in the international standards for time averaging [24], [25], SS is considered to represent the worst case in terms of temperature elevation and $1\,\text{min}$ as a typical duration of a short call or of browsing session. For the short exposure (i.e., $1\,\text{min}$), thermal diffusion can be neglected and the temperature rise is representative of the absorbed power. This is illustrated in Fig. 5 that represents the PLD averaged over the cylinder section.

The results are obtained for an incident power density of $10\,\text{W/m}^2$. At both frequencies and for both polarizations, PLD_{av} and Δ T$_{\text{av}}$ decrease when the cylinder radius increases.

It is interesting to notice that, while at 60 GHz for $a = 1\,\text{mm}$ PLD_{av} and ΔT_{av} are almost identical for both polarizations (e.g., $PLD_{\text{av}} = 5671\text{W/m}^3$ for TE and $PLD_{\text{av}} = 5840\text{W/m}^3$ for TM), at 26 GHz there is a difference of about a factor of 2 between TE and TM (PLD_{av} is 3903 W/m^3 for TE and 8203 W/m^3 for TM). This may seem to be contradictory with respect to the results described in Section III-A, where it is shown that for TE polarization $APD_{\max}$ for small radii is lower than the value obtained with the same a for TM polarization (difference of $126.32\,\%$ at 26 GHz and $32.57\,\%$ at 60 GHz for $a = 1\,\text{mm}$). However, the temperature rise depends on the total absorbed power rather than on its peak value. At 60 GHz, when $a = 1\,\text{mm}$ Figs. 4(c) and 4(d) the absorption is superficial and the difference in terms of the peak values between the two polarizations has only a limited impact on the total absorbed power. On the contrary, at 26 GHz, even if the absorption cannot be considered fully volumetric, PLD differs significantly over the whole cylinder section for the two polarizations Figs. 4(a) and 4(b).

The maximal temperature rise $\Delta T_{\max}$ is reported in Fig. 6, while some key results, showing $\Delta T_{\max}$ and the associated $\Delta APD_{\max}$, for $a = 1\,\mathrm{mm}$, $5\,\mathrm{mm}$, and $10\,\mathrm{mm}$ are summarized in Table I.

The temperature elevation is computed using the cylindrical model (Phantom 1) for $1\,\mathrm{mm} \leq a \leq 10\,\mathrm{mm}$ and the modified model (Phantom 2) for $1\,\mathrm{mm} \leq a \leq 5\,\mathrm{mm}$, representative of the ear dimensions. As expected, for both frequencies and polarizations $\Delta T_{\max}$ increases with the exposure duration and reaches its maximum at SS. All the configurations lead to a higher temperature rise for small a and tend towards the reference value of the planar interface for radii approaching $10\,\mathrm{mm}$. Similarly to Fig. 5, for all the exposure durations and $a = 1\,\mathrm{mm}$, the maximal temperature elevation is almost the same for the two polarizations at $60\,\mathrm{GHz}$ and differs by about a factor of 2 at $26\,\mathrm{GHz}$.

Contrary to $APD_{\max}$ (Fig. 2), $\Delta T_{\max}$ variations are significantly higher compared to the planar interface. As an example, these variations at SS and for $a = 1\,\mathrm{mm}$ can reach $161.51\,\%$ for TE polarization and $451.45\,\%$ for TM polarization at $26\,\mathrm{GHz}$ (Fig. 6). Under the same conditions, at $60\,\mathrm{GHz}$ $\Delta T_{\max}$ variations are of $214.41\,\%$ and $226.03\,\%$ for TE and TM polarizations, respectively. However, as discussed in Section II, for the curvature radii representative of the ears the cylindrical model is not suitable to compute the temperature elevation since the tissue portion connecting the ear with the head contributes to the heat dissipation. For this reason, $\Delta T_{\max}$ computed considering Phantom 2 is also reported in Fig. 6. The temperature rise is strongly reduced compared to the results for the cylindrical phantom due to a wider surface experiencing heat convection. In this case, for $a = 1\,\mathrm{mm}$ the variations at SS are $92.95\,\%$ (TE polarization) and $93.11\,\%$ (TM polarization) at $26\,\mathrm{GHz}$, and $103.62\,\%$ (TE polarization) and $31.65\,\%$ (TM polarization) at $60\,\mathrm{GHz}$. For $a = 5\,\mathrm{mm}$, $\Delta T_{\max}$ for Phantom 2 approaches that of Phantom 1.

It is interesting to notice that for $a = 1\,\mathrm{mm}$ after $6\,\mathrm{min}$ of exposure and at SS, the temperature rise for the TE polarization becomes comparable (at 26 GHz) or higher (60 GHz) than the one for TM when considering Phantom 2, while for Phantom 1 $\Delta T_{\max}$ is almost the same for both polarizations at $60\,\mathrm{GHz}$, and it is higher for TM than for TE at $26\,\mathrm{GHz}$. This variation relies on the fact that for TE polarization in Phantom 2 the PLD increases due to fact that the exposure is not only induced on the skin-air interface of the curved portion but also along the side with a length l, thus increasing the overall power absorbed by the tissue.

IV. Discussion and Conclusion

This study investigates the impact of the ear and finger curvature on the EM power absorption and heating at mmW frequencies upcoming for 5G and future generations, with a special attention to $26\,\mathrm{GHz}$ and $60\,\mathrm{GHz}$. To analyze the exposure levels in curved body parts we considered two homogenous skin models: (1) an infinite cylinder; (2) an infinite cylinder extended along x axis. The first one is used to evaluate the EM power density in finger (a up to $10\,\mathrm{mm}$) and ear ($1\,\mathrm{mm} \leq a \leq 5\,\mathrm{mm}$) as well as the temperature rise in the finger. The latter is used to calculate the temperature rise in the ear, to account for the thermal conduction due to the tissue connecting the ear to the head.

At $26\,\mathrm{GHz}$ and $60\,\mathrm{GHz}$, for TE polarization $APD_{\max}$ remains lower than for the planar interface case, while for TM polarization $APD_{\max}$ is higher. At 26 GHz the variations reach $-38.2\,\%$ for TE and $72.3\,\%$ for TM polarization. At $60\,\mathrm{GHz}$, the maximal increase is $15\,\%$ for TM polarization and the maximal decrease is $-18.7\,\%$ for TE polarization. As a increases $APD_{\max}$ approaches the planar interface value. This shows that at $26\,\mathrm{GHz}$ and $60\,\mathrm{GHz}$, for curvature radii comparable to the ones of the ear ($a \leq 5\,\mathrm{mm}$) the difference compared to the planar interface in terms of $APD_{\max}$ can be higher than $10\,\%$ and that this difference increases as frequency decreases due to a higher penetration depth. For a finger with a radius $a = 10\,\mathrm{mm}$ the variations are lower than $10\,\%$ at 26 GHz and $5\,\%$ at 60 GHz.

The variations of $\Delta T_{\max}$ in respect to a planar interface are significantly stronger compared to those of $APD_{\max}$. For the ear at SS they reach $92.95\,\%$ (TE polarization) and $93.11\,\%$ (TM polarization) at $26\,\mathrm{GHz}$, and $103.62\,\%$ (TE polarization) and $31.65\,\%$ (TM polarization) at $60\,\mathrm{GHz}$. Independently of the polarization the temperature increase for curved structure with a radius in the considered range ($1\,\mathrm{mm} \leq a \leq 10\,\mathrm{mm}$) leads to a temperature increase which is higher than the one for a planar interface. This is mainly due to the different thermal boundary conditions and a low heat conduction of air, which results in higher heat accumulation for curved structures due to the decrease in heat exchange with the surrounding medium.

The resulting variations of the $APD_{\max}$ are lower than the safety margins applied to exposure limits (i.e., 10 for general public and 2 for occupational exposure [24]). For small radii (i.e., of about $1\,\mathrm{mm}$), $APD_{\max}$ and $\Delta T_{\max}$ variations become higher than the ones induced by age-dependent physiological parameters ($\sim$$15\,\%$ [12]) and by the presence of a textile ($\sim$$50\,\%$ [11]). The phantoms used in this study approximate the shapes of finger and ear, which are not purely cylindrical. Our preliminary results on anatomical models—not reported in the paper for the sake of brevity—show a good agreement with the canonical phantoms (difference of $2\,\%$ in term of $APD_{\max}$ at $60\,\mathrm{GHz}$, TM polarization [28]). The detailed analysis of the impact of more realistic anatomical shapes and radiating sources on the EM exposure and temperature rise is one of the perspectives of this study and will be reported in a separate paper.

References

[1] Federal Communications Commission (FCC), "Auction 101: Spectrum frontiers — 28 GHz," Accessed: Feb. 18, 2022. [Online]. Available: https://www.fcc.gov/auction/101/factsheet

[2] European Commission, "Shaping europe's digital future," Accessed: Feb. 18, 2022. [Online]. Available: https://digital-strategy.ec.europa.eu/en/news/european-commission-harmonise-last-pioneer-frequency-band-needed-5g-deployment

[3] European Telecommunications Standards Institute (ETSI), "ETSI EN 302 567 V2.1.1 (2017–07)," 2017. Accessed: Feb. 18 2022. [Online]. Available: https://www.etsi.org/deliver/etsi_en/302500_302599/302567/02.01.01_60/en_302567v020101p.pdf

[4] Federal Communications Commission (FCC), "Fact sheet on spectrum frontiers item," Accessed: Feb. 18, 2022. [Online]. Available: https://www.fcc.gov/document/fact-sheet-spectrum-frontiers-item

[5] Infineon, "60GHz radar sensors," Accessed: Feb. 18 2022. [Online]. Available: https://www.infineon.com/cms/en/product/sensor/radar-sensors/radar-sensors-for-iot/60ghz-radar/?gclid=CjwKCAjw7vuUBhBUEiwAEdu2pP_aElHWctWCC5_ZJcQ7nO9eFu_NFDJzopE4Xxskg-JD43Mt31IR3RoCjXcQAvD_BwE&gclsrc=aw.ds

[6] Texax Instruments, "Industrial mmWave radar sensors," Accessed: Feb. 18, 2022. [Online]. Available: https://www.ti.com/sensors/mmwave-radar/industrial/overview.html

[7] A. Hirata *et al.*, "Human exposure to radiofrequency energy above 6 GHz: Review of computational dosimetry studies," *Phys. Med. Biol.*, vol. 66, no. 8, Apr. 2021, Art. no. 08TR01.

[8] T. Nakae, D. Funahashi, J. Higashiyama, T. Onishi, and A. Hirata, "Skin temperature elevation for incident power densities from dipole arrays at 28 GHz," *IEEE Access*, vol. 8, pp. 26863–26871, 2020.

[9] M. Ziane, R. Sauleau, and M. Zhadobov, "Antenna/body coupling in the near-field at 60 GHz: Impact on the absorbed power density," *Appl. Sci.*, vol. 10, no. 21, Oct. 2020, Art. no. 7392.

[10] M. C. Ziskin, S. I. Alekseev, K. R. Foster, and Q. Balzano, "Tissue models for RF exposure evaluation at frequencies above 6 GHz," *Bioelectromagnetics*, vol. 39, no. 3, pp. 173–189, Apr. 2018.

[11] G. Sacco, S. Pisa, and M. Zhadobov, "Impact of textile on electromagnetic power and heating in near-surface tissues at 26 GHz and 60 GHz," *IEEE J. Electromagn., RF, Microw. Med. Biol.*, vol. 5, no. 3, pp. 262–268, Dec. 2020.

[12] G. Sacco, S. Pisa, and M. Zhadobov, "Age-dependence of electromagnetic power and heat deposition in near-surface tissues in emerging 5G bands," *Sci. Rep.*, vol. 11, no. 1, Feb. 2021, Art. no. 3983.

[13] A. Christ, T. Samaras, E. Neufeld, and N. Kuster, "RF-induced temperature increase in a stratified model of the skin for plane-wave exposure at 6–100 GHz," *Radiat. Protection Dosimetry*, vol. 188, no. 3, pp. 350–360, Jun. 2020.

[14] W. He, B. Xu, M. Gustafsson, Z. Ying, and S. He, "RF compliance study of temperature elevation in human head model around 28 GHz for 5G user equipment application: Simulation analysis," *IEEE Access*, vol. 6, pp. 830–838, 2018.

[15] C.-H. Li, M. Douglas, E. Ofli, N. Chavannes, Q. Balzano, and N. Kuster, "Mechanisms of RF electromagnetic field absorption in human hands and fingers," *IEEE Trans. Microw. Theory Techn.*, vol. 60, no. 7, pp. 2267–2276, Jul. 2012.

[16] L. Petrillo, T. Mavridis, J. Sarrazin, D. Lautru, A. Benlarbi-Delai, and P. De Doncker, "Analytical creeping wave model and measurements for 60 GHz body area networks," *IEEE Trans. Antennas Propag.*, vol. 62, no. 8, pp. 4352–4356, Aug. 2014.

[17] Y. Diao, E. A. Rashed, and A. Hirata, "Assessment of absorbed power density and temperature rise for nonplanar body model under electromagnetic exposure above 6 GHz," *Phys. Med. Biol.*, vol. 65, no. 22, Nov. 2020, Art. no. 224001.

[18] F. S. Barnes and B. Greenebaum, "Handbook of biological effects of electromagnetic fields," *Choice Rev. Online*, Boca Ranton, USA: Taylor Francis Group, vol. 33, no. 11, pp. 33–6361–33–6361, Jul. 2006.

[19] European Telecommunications Standards Institute (ETSI), "ETSI TS 138 101–2V15.3.0 (2018-10)," 2018. Accessed: Feb. 18, 2022. [Online]. Available: https://www.etsi.org/deliver/etsi_ts/138100_138199/13810102/15.03.00_60/ts_13810102v150300p.pdf

[20] E. Cakit, B. Durgun, O. Cetik, and O. Yoldas, "A survey of hand anthropometry and biomechanical measurements of dentistry students in Turkey: Hand anthropometry and biomechanical measurements of dentistry students," *Hum. Factors Ergonom. Manuf. Serv. Industries*, vol. 24, no. 6, pp. 739–753, Nov. 2014.

[21] B. Hohendorff, C. Weidermann, K. Burkhart, P. Rommens, K. Prommersberger, and M. Konerding, "Lengths, girths, and diameters of children's fingers from 3 to 10 years of age," *Ann. Anatomy - Anatomischer Anzeiger*, vol. 192, no. 3, pp. 156–161, May 2010.

[22] C. Gabriel, "Compilation of the dielectric properties of body tissues at RF and microwave frequencies" Dept. Phys., King's College London, London, U.K., Tech. Rep. AFOSR-TR-96, Jan. 1996.

[23] J.-M. Jin, *Theory and Computation of Electromagnetic Fields*. 2nd ed. Hoboken, NJ, USA: Wiley, 2015.

[24] International Commission on Non-Ionizing Radiation Protection (ICNIRP), "Guidelines for limiting exposure to electromagnetic fields (100 kHz to 300 GHz)," *Health Phys.*, vol. 118, no. 5, pp. 483–524, May 2020.

[25] "IEEE Standard for Safety Levels With Respect to Human Exposure to Electric, Magnetic, and Electromagnetic Fields, 0 Hz to 300 GHz," IEEE Standard C95.1-2019 2019.

[26] H. H. Pennes, "Analysis of tissue and arterid blood temperatures in the resting human forearm," *J. Appl. Physiol.*, vol. 1, no. 2, pp. 93–122, Aug. 1948.

[27] P. A. Hasgall *et al.*, "IT'IS database for thermal and electromagnetic parameters of biological tissues version 4.0," May 2018. [Online]. Available: https://www.itis.swiss/virtual-population/tissue-properties/overview/

[28] A. Lojić Kapetanović, G. Sacco, D. Poljak, and M. Zhadobov, "Novel procedure for spatial averaging of absorbed power density on realistic body models at millimeter waves," in *Proc. BioEM*, Nagoya, Japan, 2022, to be published, doi: 10.1109/MMM.2014.2377587.

Giulia Sacco (Member, IEEE) received the M.S. degree (*summa cum laude*) in biomedical engineering and the Ph.D. degree (*cum laude* and with the Doctor Europaeus label) in information and communication technology from the Sapienza University of Rome, Rome, Italy, in 2017 and 2021, respectively. From April 2019 to September 2019, she was a Visiting Researcher with Stiching IMEC Eindhoven, The Netherlands. She is currently a Marie Skłodowska-Curie BIENVENÜE Fellow with Institut d'Électronique et des Technologies du Numérique, Rennes, France. Her scientific and research interests include the field of innovative biomedical applications of electromagnetic fields and radars for vital signs monitoring. Dr. Sacco was the recipient of the Bourse de jeunes chercheurs Grant at XXXIV General Assembly and Scientific Symposium of the International Union of Radio Science (Union Radio Scientifique Internationale-URSI) 2021, Best Student Paper Award at the XXXIII GASS of the International Union of Radio Science (Union Radio Scientifique Internationale-URSI) 2020, and Best Student Paper Award at Photonics and Electromagnetics Research Symposium (PIERS) 2019.

Zain Haider received the M.S. degree in electrical engineering from the National University of Sciences and Technology, Islamabad, Pakistan, in 2017. He is currently working toward the Ph.D. degree in bioelectromagnetics with the Institute of Electronics and Telecommunications of Rennes, University of Rennes 1, Rennes, France. His research interests include microdosimetry and metamaterials.

Maxim Zhadobov (Senior Member, IEEE) received the Ph.D. and Habilitation à Diriger des Recherches degrees from the Institut d'Electronique et des Technologies du Numerique (IETR), University of Rennes 1, Rennes, France, in 2006 and 2016, respectively. He was a Postdoctoral Researcher with the Center for Biomedical Physics, Temple University, Philadelphia, PA, USA, till 2008, and then joined the French National Center for Scientific Research. He is currently the Senior Research Scientist in biomedical electromagnetics with the IETR/CNRS, and the Head of the eWAVES Team, IETR. His scientific interests and research interests include innovative biomedical applications of electromagnetic fields and associated technologies. He has coauthored five book chapters, more than 80 research papers in peer-reviewed international journals and 200 contributions to conferences and workshops. His review article in the *International Journal of Microwave and Wireless Technologies* has been the most cited paper in 2016–2021. A paper published by his research group in 2019 is in Journal Top 100 of Nature Scientific Reports. He has been involved in 24 research projects (12 as PI). Dr. Zhadobov was the TPC Co-Chair of BioEM 2020/2021 conferences. He was also a TPC member and/or session organizer at IEEE IMBioC 2022, AT-AP-RASC 2022, BioEM 2019, EuMW 2019, IEEE iWEM 2017, MobiHealth 2015–2017, BodyNets 2016, and IMWS-Bio 2014. He is an elected member of EBEA Council, member of IEEE TC95.4, and the Vice-President of URSI France Commission K. He is an Associate Editor for the IEEE JOURNAL OF ELECTROMAGNETICS RF AND MICROWAVES IN MEDICINE AND BIOLOGY and was the Guest Editor of *Applied Sciences and Sensors* journals. He is a member of the Technical Advisory Committee URSI Com-K and has been acting as an Expert at research councils worldwide. He was the recipient of CNRS Medal in 2018, EBEA Award for Excellence in Bioelectromagnetics in 2015, and Brittany's Young Scientist Award in 2010. Since 2010, Ph.D. students he supervised were the recipient of seven national scientific awards and five awards from the Bioelectromagnetics Society, URSI, and IEEE Antennas and Propagation Society.